

Article

Atomistic Investigation of Titanium Carbide Ti_8C_5 under Impact Loading

Kang Xia ^{1,2,*}, Haifei Zhan ^{2,3}, Jianli Shao ⁴, Jiaqiu Wang ², Zhuoqun Zheng ⁵, Xinjie Zhang ¹ and Zhiyong Li ²

¹ College of Mechanical & Electrical Engineering, HoHai University, Nanjing 210098, China

² School of Mechanical, Medical and Process Engineering, Queensland University of Technology (QUT), Brisbane, QLD 4001, Australia

³ College of Civil Engineering and Architecture, Zhejiang University, Hangzhou 310058, China

⁴ State Key Laboratory of Explosion Science and Technology, Beijing Institute of Technology, Beijing 100081, China

⁵ State Key Laboratory of Mechanics and Control of Mechanical Structures, Nanjing University of Aeronautics and Astronautics, Nanjing 210016, China

* Correspondence: xiak@hhu.edu.cn

Abstract: Titanium carbides attract attention from both academic and industry fields because of their intriguing mechanical properties and proven potential as appealing candidates in the variety of fields such as nanomechanics, nanoelectronics, energy storage and oil/water separation devices. A recent study revealed that the presence of Ti_8C_5 not only improves the impact strength of composites as coatings, but also possesses significant strengthening performance as an interlayer material in composites by forming strong bonding between different matrices, which sheds light on the design of impact protection composite materials. To further investigate the impact resistance and strengthening mechanism of Ti_8C_5 , a pilot Molecular Dynamics (MD) study utilizing comb3 potential is carried out on a Ti_8C_5 nanosheet by subjecting it to hypervelocity impacts. The deformation behaviour of Ti_8C_5 and the related impact resist mechanisms are assessed in this research. At a low impact velocity ~ 0.5 km/s, the main resonance frequency of Ti_8C_5 is 11.9 GHz and its low Q factor (111.9) indicates a decent energy damping capability, which would eliminate the received energy in an interfacial reflection process and weaken the shock waves for Ti_8C_5 strengthened composites. As the impact velocity increases above the threshold of 1.8 km/s, Ti_8C_5 demonstrates brittle behaviour, which is signified by its insignificant out-of-plane deformation prior to crack initiation. When tracking atomic Von Mises stress distribution, the elastic wave propagation velocity of Ti_8C_5 is calculated to be 5.34 and 5.90 km/s for X and Y directions, respectively. These figures are inferior compared with graphene and copper, which indicate slower energy delocalization rates and thus less energy dissipation via deformation is expected prior to bond break. However, because of its relatively small mass density comparing with copper, Ti_8C_5 presents superior specific penetration. This study provides a fundamental understanding of the deformation and penetration mechanisms of titanium carbide nanosheets under impact, which is crucial in order to facilitate emerging impact protection applications for titanium carbide-related composites.

Keywords: titanium carbide; hypervelocity impact; stress wave propagation; molecular dynamics simulations



Citation: Xia, K.; Zhan, H.; Shao, J.; Wang, J.; Zheng, Z.; Zhang, X.; Li, Z. Atomistic Investigation of Titanium Carbide Ti_8C_5 under Impact Loading. *Metals* **2022**, *12*, 1989. <https://doi.org/10.3390/met12111989>

Academic Editor: Shengguo Ma

Received: 19 October 2022

Accepted: 17 November 2022

Published: 20 November 2022

Publisher's Note: MDPI stays neutral with regard to jurisdictional claims in published maps and institutional affiliations.



Copyright: © 2022 by the authors. Licensee MDPI, Basel, Switzerland. This article is an open access article distributed under the terms and conditions of the Creative Commons Attribution (CC BY) license (<https://creativecommons.org/licenses/by/4.0/>).

1. Introduction

In recent decades, tremendous efforts on the exploration of titanium matrix composites have been conducted because of their outstanding mechanical properties [1,2] and tuneable potential [2–6]. Titanium carbide is a widely adopted strengthening material in composites and has received immense attention from civil automobile, aerospace as well as military industries, owing to its superior bending rigidity [7], Young's modulus [8], strength to weight ratio, wear and corrosion resistance [9], Oil/water separation capability [10], etc. To

this end, an in situ synthesis of titanium carbide is realized via multiple approaches such as supersonic flame spraying process [11], high temperature and high-pressure environment synthesis [12], low temperature salt bath carburizing [13] and state-of-art high energy beam setups, such as laser cladding [14]. Micro-meter titanium carbide can be achieved via the dissolution-precipitation mechanism utilizing a high-energy laser.

Varieties of titanium carbides have been successfully realized so far; however, constrained by the lateral size of sheets and complex oxygen-containing function groups observed in the state-of-art synthesis process, most studies on monolithic titanium carbides have been carried out via in silico approaches such as Molecular Dynamics (MD) and Density Function Theory (DFT)-based simulation [15]. Deploying an empirical potential energy function and embedded atom method, a MD study suggests the bending rigidity of 2D titanium carbides can be as high as ~49.55 eV, which is much more significant than graphene and MoS₂ (2.3 and 9.61 eV, respectively) [7]. A DFT study on functionalized titanium carbides suggests that the oxygen group not only enhances ideal strength, but also induces a strong anisotropy for titanium carbides as the material subjected to tensile loading [16]. Recently, a follow-up MD study utilizing COMB3 potential confirmed the above findings; moreover, the Young's modulus of the assessed titanium-based carbides ranged between 133 and 517 GPa, which shows its potential in nanomechanics, nanoelectronics and energy storage applications [8].

In addition to having outstanding mechanical properties, pristine titanium carbides are also known for their strengthening material/matrix in varieties of composites. Titanium carbide (Ti₈C₅) thin film on a Ti₆Al₄V alloy surface realized via low temperature carburizing salt bath possesses significantly improved friction and wear properties and its surface hardness reaches ~953.28HV, which is 1.57 times higher than Ti₆Al₄V [13]. Moreover, Ti₈C₅ nanolayers/nanoparticles in situ formed at an interface of RGO/CuTi composite function as 'rivets' show sizes of up to ~100 nm. The presence of these Ti₈C₅ 'rivets' raises the interfacial strength, increases load transfer efficiency between layers and clearly presents a 53.9% improvement in tensile strength compared with composites without Ti₈C₅ in their interface [12]. The strengthening behaviour is also confirmed by a study on CNTs/Cu-Ti composites with strong Ti₈C₅ interfacial bonding [17]. Moreover, the quasi-static loading experiments' shock loading result states that Ti₈C₅ formed between diamond and titanium under a sintering temperature improves the impact strength of diamonds as coatings, which clearly suggests their impact protection potential [18].

Considering the mechanical strengthening behaviour of Ti₈C₅ in composites (such as graphene-copper composite) under quasi-static uniaxial tensile loading, its performance under various impact loading condition is rarely systematically discussed in the literature; however, it is critical to facilitate its application in bullet-proof fields as well as promote the interface design of advanced composites for impact resist applications [12,19,20]. Because of the experimental manipulation complex and small lateral dimensions of available Ti₈C₅ sheets [12], a pilot study on impact resistance of Ti₈C₅ under various impact velocities is carried out utilizing the MD method. In this study, resonance pattern, stress distribution capability as well as the specific penetration energy of Ti₈C₅ are accessed. The performance and phenomenon of a Ti₈C₅ nanosheet under impact loading are mainly compared with a thin copper layer and single-layer graphene in this pilot study.

2. Materials and Methods

The mechanical behaviour of Ti₈C₅ under hypervelocity impact was assessed through a series of large-scale MD simulations performed with the aid of the open-source package LAMMPS [21]. A spherical diamond projectile with a radius of 25 Å and a square 50 × 50 nm² Ti₈C₅ nanosheet [22] were considered. The (010) plane of the Ti₈C₅ nanosheet faced the projectile. Initial velocities ranging from 5 to 70 Å/ps (i.e., 0.5–7 km/s) were assigned to the projectiles. The boundaries of the Ti₈C₅ nanosheets were fixed during the impact process (Figure 1a), whereas the projectile was located above the centre of the Ti₈C₅ sample with an initial distance of ~20 Å. Considering the high thermal fluctuations gener-

ated during the impact process, the simulation temperature was set to be 10 K. Simulations with higher environment temperatures up to 700 K were also performed for validation, whereby the obtained penetration energy for the same impact velocities was maintained at the same level (Supplementary Materials, Figure S1). However, noting the negative correlation between temperature and material strength [23,24], a further increase to the environmental temperature may lead to lower penetration energy. A time step of 0.1 fs was selected for the simulations.

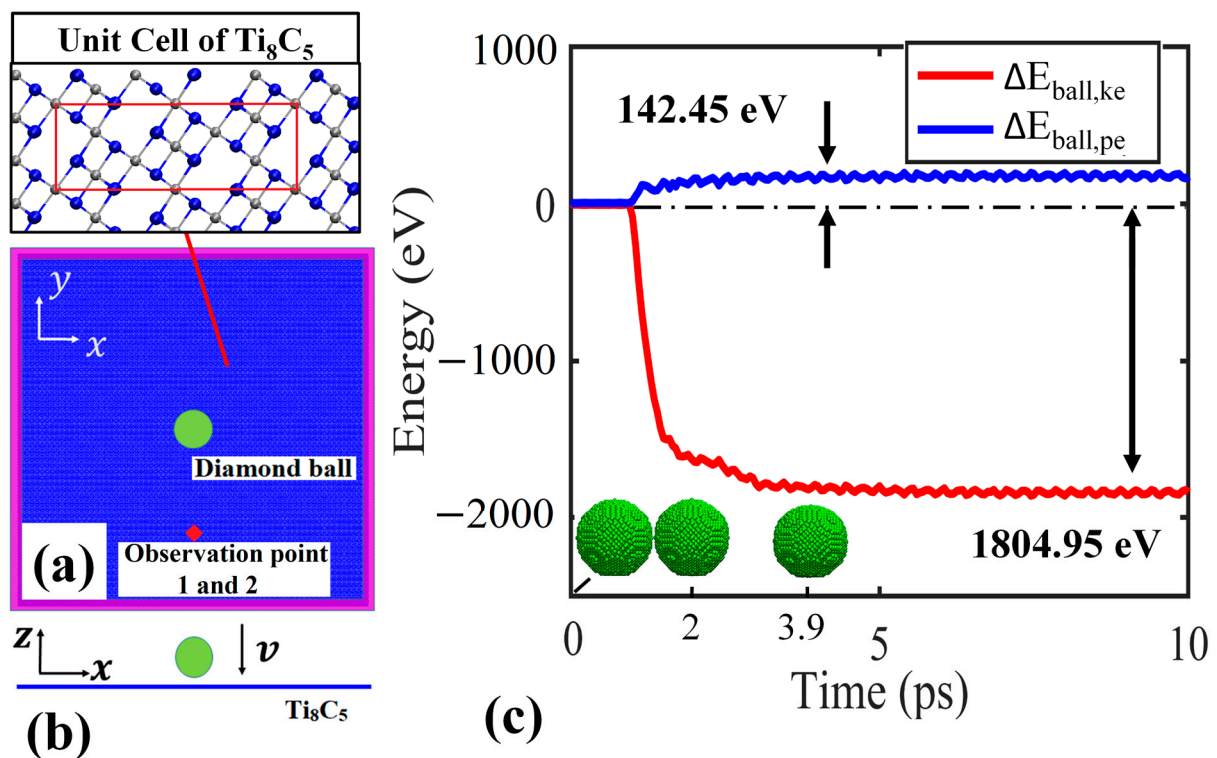


Figure 1. Impact simulation setup for the Ti_8C_5 model, (010) with the plane of the Ti_8C_5 facing the projectile. (a) Top view of the schematic setup. Insert shows the unit cell thickness of the (001) plane Ti_8C_5 , and atoms labelled in silver and blue are carbon and titanium, respectively; (b) Side view of the schematic setup; the thickness of the model is equal to the thickness of the Ti_8C_5 unit cell; (c) Energy change in projectile as a function of time for impact velocity of 2 km/s. $\Delta E_{\text{ball,ke}}$ and $\Delta E_{\text{ball,pe}}$ represent the kinetic and potential energy change of the projectile, respectively. The green balls represent the diamond projectile at a simulation time of 0, 2 and 3.9 ps. Significant deformation is not observed in the projectile during the impact process.

The third generation Charge-Optimized Many-Body potential (COMB3) was employed to describe the C-Ti atomic interactions in the Ti_8C_5 nanosheet, as well as the Cu-Cu interaction in copper, as it was fully optimized in order to determine the binding energy of carbon- and metal-based systems [25–29]. The COMB3 potential is defined as follows,

$$E_{\text{COMB3}} = V^{\text{ES}} + V^{\text{SHORT}} + V^{\text{vdW}} + V^{\text{CORR}} \quad (1)$$

where V^{ES} is an electrostatic term, which is the sum of atomic ionization energies and energy related to the Coulomb interaction. V^{SHORT} , V^{vdW} and V^{CORR} represent the short range, van der Waals and correction energy term, respectively. The Tersoff potential was utilized to simulate the atomic interactions in diamonds, which has been shown to describe the binding energy for carbonaceous system well [30]. The interactions between the diamond projectile and nanosheets were described by Morse potential [31]. Prior to the impact process, a conjugate gradient algorithm was applied to conduct energy minimization, and then the Nose–Hoover thermostat [32] was employed to equilibrate the whole system at

10 K for 2000 fs under the canonical ensemble. The equations of motion were integrated with time using the velocity Verlet algorithm [33] and no periodic boundary conditions were adopted. To reproduce the energy conversion from kinetic energy to potential energy, no thermostat was applied during the impact process. During the simulation, the atomic stress was calculated based on the virial stress $\Pi^{\alpha\beta}$ [34],

$$\Pi^{\alpha\beta} = \frac{1}{\Omega} \sum_i \omega_i \pi_i^{\alpha\beta}, \quad \pi_i^{\alpha\beta} = \frac{1}{\omega_i} \left(-m_i v_i^\alpha v_i^\beta + \frac{1}{2} \sum_{j \neq i} F_{ij}^\alpha r_{ij}^\beta \right) \quad (2)$$

Here, $\pi_i^{\alpha\beta}$ is the atomic stress associated with atom i . ω_i is the effective volume of the i th atom and Ω is the volume of the whole system. m_i and v_i are the mass and velocity of the i th atom, respectively. F_{ij} and r_{ij} are the force and distance between atoms i and j , respectively, and the indices α and β denote the Cartesian components. The volume of the Ti_8C_5 nanosheet is estimated by assuming the Ti_8C_5 as a continuum media with a thickness of h (13.6 Å). Considering that adopting different atomic volumes will alter the magnitude of the stress, it will not however change the trends of the results as focused on in this paper. Considering the complex stress states during impact, we tracked the Von Mises stress σ_{VM} in the nanosheet based on the atomic virial stress (Equation (2)), as calculated by

$$\sigma_{VM} = \sqrt{((\sigma_x - \sigma_y)^2 + (\sigma_y - \sigma_z)^2 + (\sigma_x - \sigma_z)^2 + 6(\sigma_{xy}^2 + \sigma_{xz}^2 + \sigma_{yz}^2))/2} \quad (3)$$

Initially, we focused on the impact performance of the Ti_8C_5 nanosheet under the impact velocity of 3 km/s. In the ideal vacuum condition, the total energy change in the projectile equals the change in the Ti_8C_5 nanosheet. It is notable that during the impact process, although the projectile exhibited an ignorable deformation, a notable amount of potential energy change in the projectile ($\Delta E_{ball,pe}$) was observed during the impact with Ti_8C_5 (Figure 1b). After perforation, the total energy loss in the projectile ($\Delta E_{ball,tot}$ which is the sum of $\Delta E_{ball,pe}$ and $\Delta E_{ball,ke}$) remains constant (Figure 1c); thus, $\Delta E_{ball,tot}$ is taken as the penetration energy (E_p) [35,36]. It was noticed that the NVE ensemble was adopted in the impact process and total energy of the system was constant during the impact process, and the energy loss in the projectile was equal to the energy gain in the nanosheet $\Delta E_{NS,tot}$ (where $\Delta E_{NS,tot}$ equals the sum of nanosheet potential energy gain ΔPe_{NS} and kinetic energy gain of nanosheet ΔKe_{NS}). As such, $E_p = \Delta E_{ball,tot} = \Delta E_{ball,pe} + \Delta E_{ball,ke} = \Delta E_{NS,tot} = \Delta Pe_{NS} + \Delta Ke_{NS}$.

3. Results and Discussion

3.1. Deformation Characteristics

To acquire the deformation process, Figure 2a–c (top panel) illustrates the atomic configurations of Ti_8C_5 at different deformation stages, namely the crack initiation, crack expansion and fully developed cracks, and the results are compared with the copper nanosheet that has a similar number of atom layers under the same experiment setup (Figure 2d–f). As expected, the crack initiates at the geometry centre, where accumulation of stress is observed. The nanosheet experiences insignificant out-of-plane deformation ~ 11.49 Å prior to the propagation of cracks and stress (Figure 2a) compared with copper (Figure 2d) and carbonaceous nanosheets [36–38], which signifies brittle behaviour. During the crack propagation phase, the stress that accumulates around the impact region starts to re-distribute and the stress distribution in the deformed region of Ti_8C_5 exhibits a circular pattern (Figure 2b,c), whereas copper (lattice orientation is [100], [010], [001] for x , y and z direction respectively) demonstrates an X-shaped pattern in the highlighted region (Figure 2d–f). In addition to the stress accumulation, dislocation is also often observed in this highlighted region. This phenomenon is considered as a result of the lattice structure and lattice orientation. Unlike the armchair and zigzag kicking fracture mechanisms observed in carbonaceous nanosheets [36–38], the cracks in Ti_8C_5 and copper propagate along all directions and the same crack shape is roughly maintained during the whole

process. Full perforation of Ti_8C_5 takes place at ~ 4.0 ps, which is significantly earlier than copper and the fully developed cracks for Ti_8C_5 are $\sim 16.8\%$ bigger than copper in terms of radius (Figure 2c).

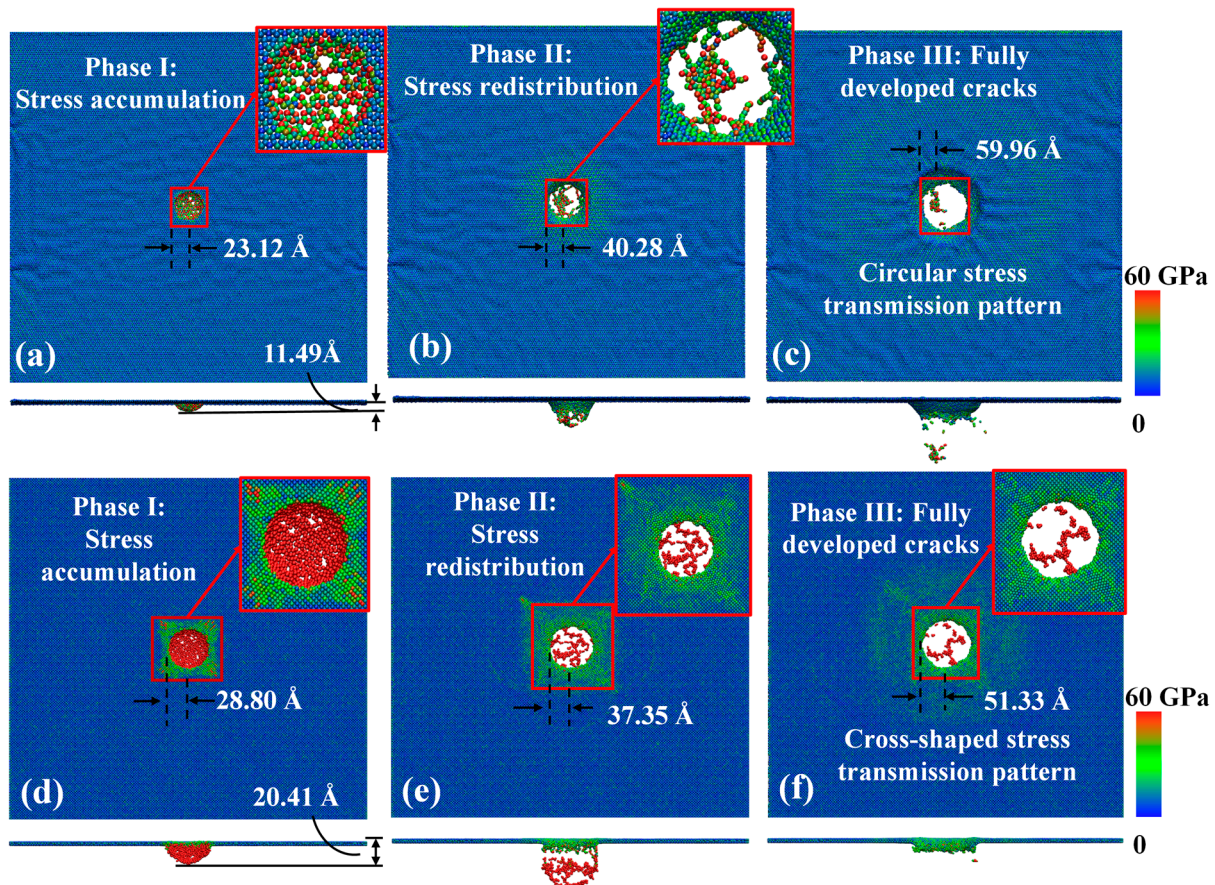


Figure 2. Von Mises stress distribution of nanosheets under impact velocity of 3 km/s. (a–c) Atomic configuration of Ti_8C_5 : (a) Von Mises stress distribution pattern at a simulation time of 1.3 ps; the insert represents stress accumulation and formation of cracks in the impact region; (b) Stress redistribution/propagation at a simulation time of 2.3 ps; (c) Final atomic configuration at 4.0 ps. (d–f) Atomic configuration of copper: (d) Von Mises stress distribution pattern at a simulation time of 2.0 ps; (e) Stress propagation phase at 3.0 ps; (f) final atomic configuration at 6.0 ps.

Higher impact velocity induces more severe local deformation. As such, extensive elastic deformation of the nanosheet is not expected. When tracking the number of discrete debris in nanosheets after the crack propagation stage (Figure 3), it presents a positive correlation with impact velocity. For an ultra-high impact velocity ~ 6 km/s, the contact region melts immediately as the projectile reaches the nanosheet and creates more discrete debris for all the cases presented in Figure 3. Among all tested samples, Ti_8C_5 generally presents a higher number of discrete debris in all examined impact velocity amplitudes. Moreover, for nanosheets subject to the high impact velocity of 6 km/s, most debris of Ti_8C_5 tends to be comprised of smaller atom groups (compared with copper), whereas the debris of graphene is more likely to be comprised of discrete atoms. Additionally, we conducted additional simulations by varying the time step from 0.1 fs to 0.5 fs, from which the same results were obtained.

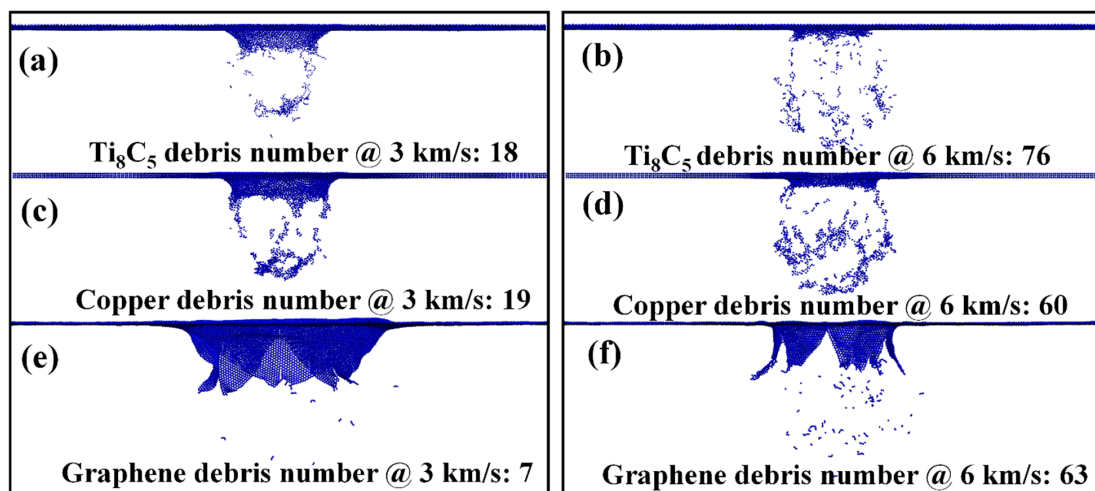


Figure 3. Impact deformation and discrete debris of nanosheets under various impact velocities. Amount of debris after impact for (a,b) Ti_8C_5 , (c,d) Copper and (e,f) Graphene are presented, respectively.

3.2. Resonance and Damping

Energy dissipation associated with resonance and damping are rarely discussed in the past shock loading or hyper velocity impact studies; however, these characteristics are essential for strengthening the matrix in laminar composites, as materials with different resonance frequencies and outstanding quality factors (Q) could eliminate the energy in the interfacial reflection process and weaken shock waves [20,39]. Utilizing the same experiment set up for all cases, oscillations in a relatively short period of 10 ps generated via various velocity impacts are recorded for amplitude and frequency comparisons. Two close observation points labelled in Figure 1a are selected for all the cases, ensuring that the captured oscillation is not influenced by crack propagation. Generally, increasing the impact velocity, oscillation amplitude and frequency does not cause significant variations in all cases. In addition, compared with graphene (Figure 4c,d) and copper (Figure 4e,f) nanosheets, Ti_8C_5 (Figure 4a,b) has significantly lower vibrational frequencies and higher amplitudes.

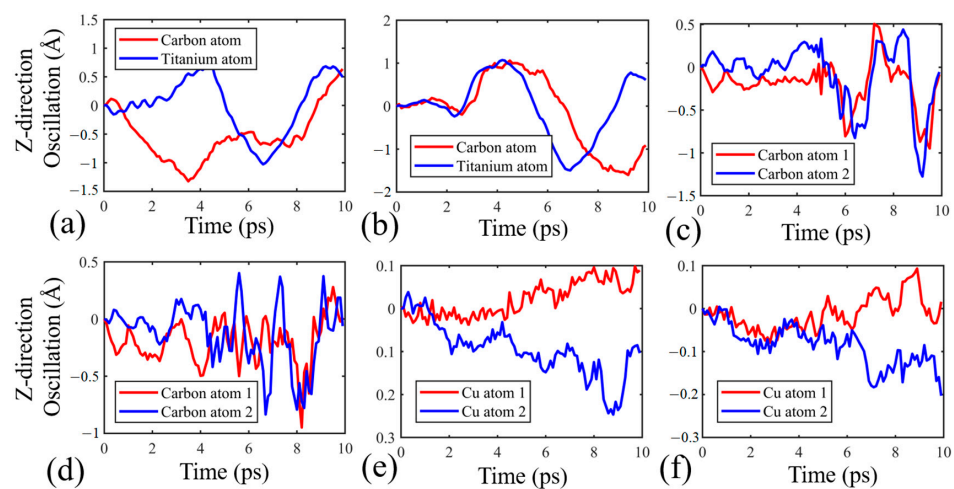


Figure 4. Z-direction oscillation of adjacent carbon and titanium atoms located at the highlighted position in Figure 1a of the Ti_8C_5 nanosheet under impact velocities of (a) 3 km/s and (b) 6 km/s; z-direction oscillation of 2 carbon atoms in graphene nanosheets (similar position as the Ti_8C_5) under impact velocities of (c) 3 km/s and (d) 6 km/s, respectively; z-direction oscillation of 2 copper atoms (similar position as the Ti_8C_5) under impact velocities of (e) 3 km/s and (f) 6 km/s, respectively.

For a more quantitative vibrational evaluation and to calculate the energy dissipation capability of the Ti_8C_5 nanosheet due to the damping process, nanosheets are subjected to a low impact velocity of 0.5 km/s, which do not penetrate the nanosheets or damage the lattice structure significantly. In all simulation scenarios, projectiles bounce back after contact. In such assessments, the external energy of nanosheets right after the departure of the projectile is recorded (Figure 5) for the calculation of the Q factor based on estimation schemes derived by previous researchers [40,41]. Here, external energy is the difference of Ti_8C_5 potential energy before and after the separation of the two objects. Q is defined as the ratio between the total system energy and the average energy loss in one radian at resonant frequency, i.e., $Q = 2\pi E_v / \Delta E_v$, where E_v is the total energy of the vibrating system and ΔE_v is donated as the dissipated energy in one cycle of vibration. Q is assumed to be constant during vibration; therefore, the correlation between maximum energy ($E_{v,n}$) after the n vibration cycles and initial energy ($E_{v,0}$) in the first vibration cycle can be denoted as $E_{v,n} = E_{v,0}(1-2\pi/Q)^n$. According to the external energy change of Ti_8C_5 presented in Figure 5a, a clear decay pattern is determined. It was noticed that the NVE ensemble adopted in this study and total energy in the vibration phase is constant, and the loss in potential energy contributes to both kinetic energy and the temperature rise of the system. Because of the remarkable decay of the oscillation amplitude, the Q factor of Ti_8C_5 possesses a small value of ~ 111.9 , and the corresponding main resonance frequency for Ti_8C_5 is calculated via discrete Fourier transform, being ~ 11.9 GHz (Figure 5b). For the graphene and copper nanosheet impact simulation, their main resonance frequencies were ~ 34.01 GHz and ~ 43.03 GHz, respectively, whereas the Q factors were 413.37 and 137.17, respectively. Considering the external energy variation and Q Factor in the 600 ps time domain, Ti_8C_5 clearly demonstrates a better damping capability over single layer graphene. Although the Q factor calculation results can be affected by the presence of a fixed boundary, all the simulations were conducted with the same fixed boundary setup, which guarantees a fair comparison.

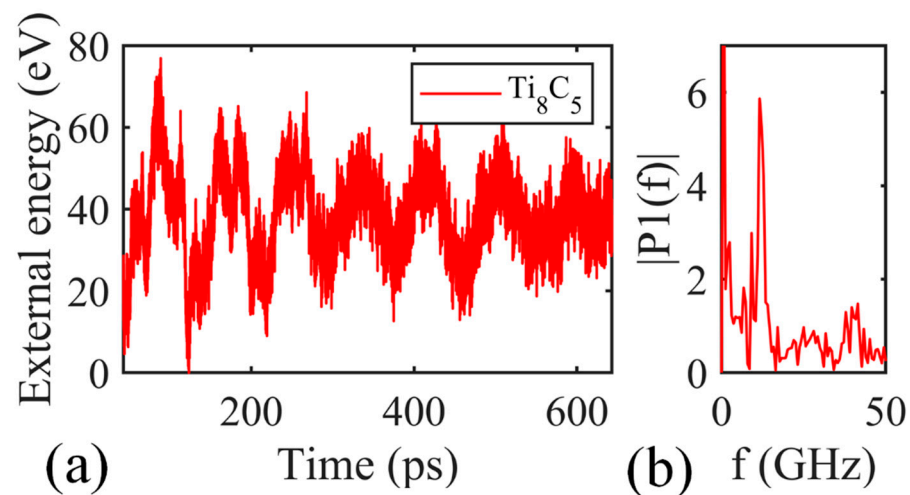


Figure 5. Oscillation of external energy of nanosheet after the separation of projectile and nanosheet. (a) External energy variation of Ti_8C_5 over time period of 600 ps and (b) The corresponding frequency spectrum of Ti_8C_5 over time period of 600 ps.

3.3. Stress Distribution and Propagation

The above discussion illustrates the morphology of Ti_8C_5 under impact. It is of great interest to compare how the stress distribution and propagation pattern in Ti_8C_5 would be altered with the variation velocity amplitudes from a more statistical point of view. In this regard, the Von Mises atomic stress distribution and elastic stress wave propagation under different impact velocities are studied as they largely determine the impact resist performance. For a lower impact velocity of 3 km/s, stress throughout the Ti_8C_5 nanosheet

prior to bond break presents a multimodal distribution pattern (Figure 6a). The main body of the data centred around 19 GPa is mainly due to impact whereas the peak on the left side is created by the fixed boundaries. As the impact increases, the peak on the left maintains the same level, whereas the mode of the main body decreases with its tail shifts towards the right (Figure 6b–d). Higher impact velocities lead to more severe stress concentrations around the impact region; moreover, stress distribution prior to bond breakage is dominated by the elastic stress propagation velocity, as the impact velocity rises much higher than the stress propagation rate, and ‘less connection’ between the main body and the tail is observed. Cumulative density function (CDF) presented in Figure 6e summaries the finding: the slope of each curve is inversely correlated with the impact velocity.

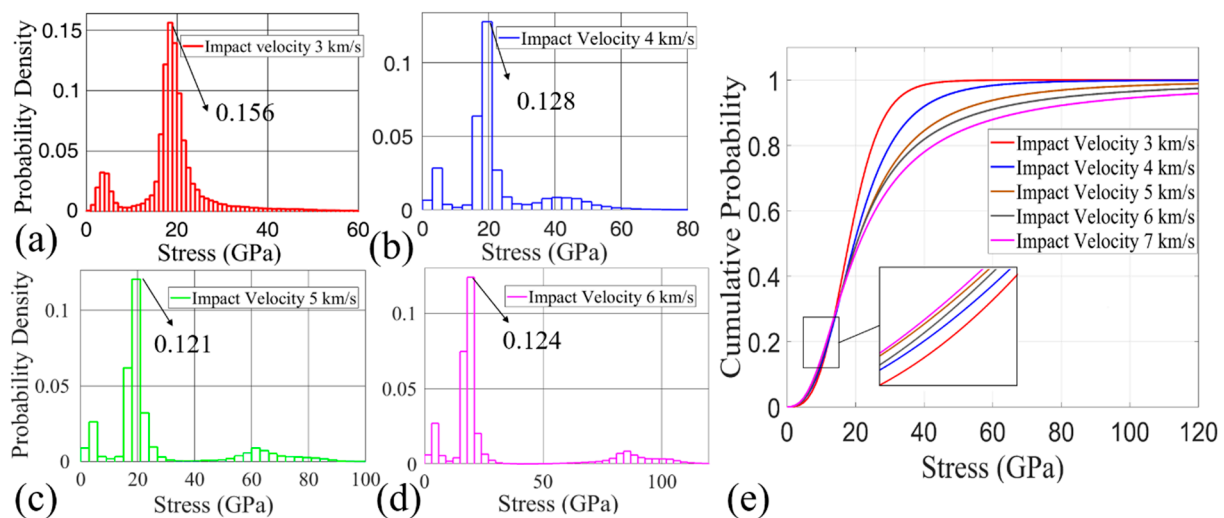


Figure 6. Von Mises atomic stress distribution of Ti_8C_5 prior to bond break, when it subject to impact velocity: (a) 3 km/s; (b) 4 km/s; (c) 5 km/s; (d) 6 km/s. (e) Cumulative density function (CDF) of the Von Mises atomic stress distribution before the crack initiation for different nanosheets under diverse impact velocities.

A nanosheet with a more significant elastic wave propagation velocity transfers momentum at a superior rate; thus, a more even stress distribution/energy delocalization is expected during ballistic impact. Theoretically, the elastic stress wave velocity v_s in a solid material can be calculated based on its Young’s modulus γ and density ρ according to $v_s = \sqrt{\gamma/\rho}$ [42,43]. In this study, v_s is estimated via tracking the location of the highest Von Mises atomic stress, as studies suggests decent agreement between the two approaches [38]. The elastic wave propagation velocity for Ti_8C_5 is 5.34 and 5.90 km/s for X and Y directions, respectively, which presents a significant gap considering copper is 7.91 (along [100] direction) and 7.52 km/s (along [010] direction). As a result, a more evenly distributed pattern throughout the nanosheet is captured at the same time instance (Figure 7a) compared with Ti_8C_5 (Figure 6a). Graphene possesses the highest elastic wave propagation velocity, which is 20.11 and 19.84 km/s along the armchair and zigzag directions, respectively; as such, its stress distribution shows a unimodal shape (Figure 7b). Slopes of the three curves in the cumulative probability diagram indicate graphene and copper are likely to bear more loading prior to bond break, and it also suggests that Ti_8C_5 owns the least significant breaking stress among all the three materials.

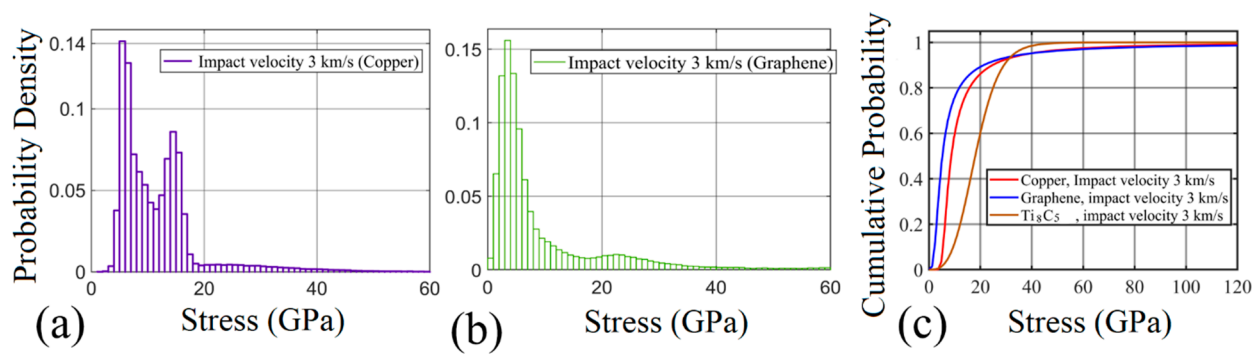


Figure 7. Stress distribution diagram for (a) copper and (b) graphene subject to an impact velocity of 3 km/s; (c) Cumulative density function (CDF) of the Von Mises atomic stress distribution before the crack initiation for different nanosheets under an impact velocity of 3 km/s (red, blue and brown lines represent copper, graphene and Ti₈C₅, respectively).

3.4. Impact Resistance Evaluation

To quantitatively evaluate the impact resistance of Ti₈C₅, its penetration (E_p) and specific penetration energy, E_p^* , under various velocity amplitudes are calculated and compared with graphene and copper. According to Figure 8a, the penetration energy of both Ti₈C₅ and copper show a consistent rate of growth in the whole velocity domain, whereas graphene experiences a notable slump in E_p at a relatively low impact velocity, which is due to the reduction in overall defamation [36]. After increasing the impact above 3 km/s, the same overall ranking is maintained. For all impact velocities, copper presents the most significant E_p and the gap between each category enlarges with impact velocity. Projectiles are not rigid bodies in this study; as a result, cracks in projectiles are found during the process if they were assigned ultra-high velocities (i.e., copper is impacted at 7 km/s).

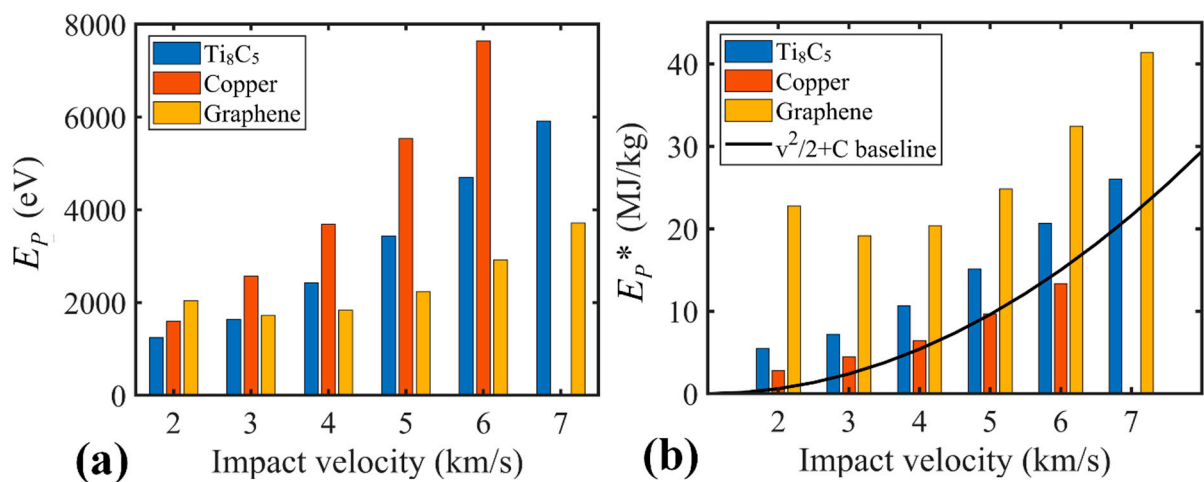


Figure 8. Performance of nanosheets' impact with projectiles of various velocity amplitudes. (a) Penetration energy and (b) Specific penetration energy as a function of impact velocity for Ti₈C₅, graphene and Copper nanosheets.

Theoretically, for nanosheets with thickness h , which is far less than projectile diameter D , i.e., $D/h \gg 1$ [44], it is regarded as a thin film and its penetration energy can be estimated by $E_p = \Delta Pe_{NS} + \Delta Ke_{NS} = (\rho A_s h)v^2/2 + E_d$. The term $(\rho A_s h)v^2/2$ refers to the minimum inelastic energy or kinetic energy transferred to the target nanosheet (where A_s represents the strike face area and v stands for the impact velocity) and the second term E_d represents other energy dissipation mechanisms such as elastic deformation or breakage of bonds. Considering the different morphology, mass as well as density differences of

various nanosheets, specific or gravimetric penetration energy is adopted to evaluate their impact resistance capability, which is calculated as $E_p^* = E_p / (\rho A_s h)$ and it can be further expressed as $E_p^* = v^2/2 + E_d^*$. Apparently, E_d^* is a figure of merit to evaluate the impact energy delocalization ability, which is dominated by elastic wave propagation velocity. Better energy delocalization ability prevents the development of local severe stress and helps the material to deform more locally prior to the arrival of bond break stress.

E_p^* in each group follows the material-independent energy dissipation baseline (i.e., $v^2/2$), and the overall ranking differs from the penetration energy (Figure 8a,b). At low impact velocities, ~ 2 km/s graphene shows superiority over the other two materials in terms of specific penetration energy, because of its most significant local deformation prior to bond break and, hence, a larger E_d^* term is expected, which is confirmed by the energy breakdown presented in Figure 9. For low impact velocities < 3 km/s, graphene shows a more significant $\Delta Pe_{NS} / \Delta E_{NS,tot}$ ratio compared with the other two nanosheets. As impact velocity increases above 3 km/s, the elastic wave propagation velocity or energy delocalization ability becomes less dominant in determining the impact resistance, as all samples experience less overall deformation prior to bond break with a less significant $\Delta Pe_{NS} / \Delta E_{NS,tot}$ ratio observed. As a result, an increase in impact velocity closes the specific penetration energy gap between graphene and Ti_8C_5 .

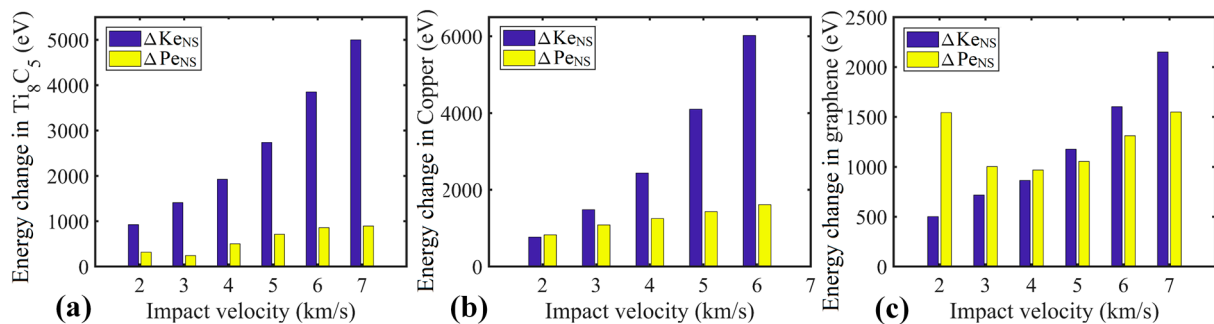


Figure 9. Energy breakdown for various nanosheets at the moment of perforation. Figures (a–c) represent the kinetic energy gain (ΔKe_{NS}) and the potential energy gain (ΔPe_{NS}) for Ti_8C_5 , copper and the graphene nanosheet, respectively.

4. Conclusions

In summary, the fracture behaviour of monolayer Ti_8C_5 subject to various hypervelocity impacts is explored. For Ti_8C_5 under relatively a low impact velocity ~ 0.5 km/s, its main resonance frequency is 11.9 GHz, which is different from other matrices in composites such as copper and graphene. A resonance study on Ti_8C_5 also shows a low Q factor of 111.9 indicates decent energy damping capability. The combination of resonance frequency and low Q factor would help to eliminate energy in the interfacial reflection process and weaken shock waves for Ti_8C_5 -strengthened composites. When increasing the impact velocity above the threshold of 1.8 km/s, a crack initiates at the geometry centre and the nanosheet experiences significant out-of-plane deformation before the propagation of the crack, demonstrating brittle behaviour. Elastic wave propagation velocity is an important figure in impact resistance assessments, as it positively correlates with the energy delocalization rate, which helps materials to deform more prior to bond break and thus absorb more energy. Tracking atomic Von Mises stress distribution, the elastic wave propagation velocity of Ti_8C_5 is calculated to be 5.34 and 5.90 km/s for X and Y directions, respectively, but these figures are not significant compared with graphene and copper, suggesting inferior energy delocalization rates and thus less energy dissipation via deformation prior to bond break. However, because of its relatively small mass density compared with copper, Ti_8C_5 presents superior specific penetration for all tested velocity amplitudes. This study provides a fundamental understanding of the deformation and penetration mechanisms of titanium carbide nanosheets under impact, which should shed lights on the design of

titanium carbide- related composites for bullet-proof applications or shielding structures for aerospace systems' protection applications for titanium carbide-related composites. We note that although these results are obtained from a Ti_8C_5 nanosheet with a small size, similar failure mechanisms are also expected for monolithic Ti_8C_5 nanosheets with a large scale.

Supplementary Materials: The following supporting information can be downloaded at: <https://www.mdpi.com/article/10.3390/met12111989/s1>, Figure S1: The penetration profile for Ti_8C_5 nanosheet subjected to impact velocity of 3 km/s. (a) Penetration energy of Ti_8C_5 nanosheet with environment temperature up to 700 K. (b) Ti_8C_5 nanosheet deformation with environment temperature of 10 K at simulation time of 2.8 ps. (c) Ti_8C_5 nanosheet deformation with environment temperature of 700 K at simulation time of 2.8 ps.

Author Contributions: Conceptualization, K.X. and H.Z.; methodology, K.X.; software, K.X.; validation, K.X. and H.Z.; formal analysis, K.X.; data curation, K.X.; writing—original draft preparation, K.X.; writing—review and editing, K.X., H.Z., J.S., J.W., Z.Z. and X.Z.; visualization, K.X.; supervision, Z.L. All authors have read and agreed to the published version of the manuscript.

Funding: This research is funded by the National Natural Science Foundation of China (12102127), Natural Science Foundation of Jiangsu Province (BK20190164), Fundamental Research Funds for the Central Universities (B210202125), the China Postdoctoral Science Foundation (2021M690872) and Changzhou Health Commission Technology Projects (ZD202103).

Institutional Review Board Statement: Not applicable.

Informed Consent Statement: Not applicable.

Data Availability Statement: Not applicable.

Conflicts of Interest: The authors declare no conflict of interest.

References

1. Fang, M.; Han, Y.; Shi, Z.; Huang, G.; Song, J.; Lu, W. Embedding boron into Ti powder for direct laser deposited titanium matrix composite: Microstructure evolution and the role of nano-TiB network structure. *Compos. B* **2021**, *211*, 108683. [[CrossRef](#)]
2. Wen, Y.; Wu, Y.; Hua, L.; Xie, L.; Wang, L.; Zhang, L.-C.; Lu, W. Effects of shot peening on microstructure evolution and mechanical properties of surface nanocrystal layer on titanium matrix composite. *Mater. Des.* **2021**, *206*, 109760. [[CrossRef](#)]
3. Xie, L.; Wu, Y.; Yao, Y.; Hua, L.; Wang, L.; Zhang, L.-C.; Lu, W. Refinement of TiB reinforcements in TiB/Ti-2Al-6Sn titanium matrix composite via electroshock treatment. *Mater. Charact.* **2021**, *180*, 111395. [[CrossRef](#)]
4. Xie, H.; Jin, Y.; Niu, M.; Liu, N.; Wang, J. Effect of Tribofilm Induced by Nanoparticle Addition on Wear Behavior of Titanium-Matrix Composite. *Tribol. Lett.* **2021**, *69*, 18. [[CrossRef](#)]
5. Niu, X.; Liu, Y.; Chen, X.; Liu, J.; Sun, Z.; Song, Y. Growth behavior of short fatigue cracks in a unidirectional SiC fiber-reinforced titanium matrix composite under spectrum loading. *Theor. Appl. Fract. Mech.* **2021**, *114*, 102980. [[CrossRef](#)]
6. Niu, H.Z.; Yin, B.G.; Zhang, H.R.; Zang, M.C.; Tan, H.; Zhang, D.L. Multiphase polymorphic nanoparticles reinforced titanium matrix composite produced by selective electron beam melting of a prealloyed composite powder. *Scr. Mater.* **2021**, *200*, 113916. [[CrossRef](#)]
7. Borysiuk, V.N.; Mochalin, V.N.; Gogotsi, Y. Bending rigidity of two-dimensional titanium carbide (MXene) nanoribbons: A molecular dynamics study. *Comput. Mater. Sci.* **2018**, *143*, 418–424. [[CrossRef](#)]
8. Hatam-Lee, S.M.; Esfandiari, A.; Rajabpour, A. Mechanical behaviors of titanium nitride and carbide MXenes: A molecular dynamics study. *Appl. Surf. Sci.* **2021**, *566*, 150633. [[CrossRef](#)]
9. Rao, V.R.; Ramanaiyah, N.; Sarcar, M.M.M. Tribological properties of Aluminium Metal Matrix Composites (AA7075 Reinforced with Titanium Carbide (TiC) Particles). *Int. J. Adv. Sci. Technol.* **2016**, *88*, 13–26. [[CrossRef](#)]
10. Li, Z.-K.; Liu, Y.; Li, L.; Wei, Y.; Caro, J.; Wang, H. Ultra-thin titanium carbide (MXene) sheet membranes for high-efficient oil/water emulsions separation. *J. Membr. Sci.* **2019**, *592*, 117361. [[CrossRef](#)]
11. Guo, J.; Xia, C. Wear Behavior and Mechanism of Thermal Sprayed TiC-NiCr Coating. *Nonferrous Met. Eng.* **2021**, *11*, 48–53.
12. Chu, K.; Wang, F.; Wang, X.-H.; Li, Y.-B.; Geng, Z.-R.; Huang, D.-J.; Zhang, H. Interface design of graphene/copper composites by matrix alloying with titanium. *Mater. Des.* **2018**, *144*, 290–303. [[CrossRef](#)]
13. Liu, X.; Liu, L.; Sun, B.; Li, B.; Ke, X. The preparation of titanium carbide thin film of Ti6Al4V at low temperature and study of friction and wear properties. *J. Meas. Eng.* **2016**, *4*, 167–172.
14. Zhou, L.; Liu, Y.; Dong, S.; Zhu, L.; Li, Y. Synthesis of Titanium Carbide Particle in Laser Melted-pool in situ. *J. Wuhan Univ. Technol. Sci. Ed.* **2020**, *34*, 1315–1320. [[CrossRef](#)]

15. Borysiuk, V.N.; Mochalin, V.N.; Gogotsi, Y. Molecular dynamic study of the mechanical properties of two-dimensional titanium carbides $Ti_n + 1C_n$ (MXenes). *Nanotechnology* **2015**, *26*, 265705. [[CrossRef](#)]
16. Fu, Z.H.; Zhang, Q.F.; Legut, D.; Si, C.; Germann, T.C.; Lookman, T.; Du, S.Y.; Francisco, J.S.; Zhang, R.F. Stabilization and strengthening effects of functional groups in two-dimensional titanium carbide. *Phys. Rev. B* **2016**, *94*, 104103. [[CrossRef](#)]
17. Xiong, N.; Bao, R.; Yi, J.; Tao, J.; Liu, Y.; Fang, D. Interface evolution and its influence on mechanical properties of CNTs/Cu-Ti composite. *Mater. Sci. Eng. A* **2019**, *755*, 75–84.
18. Mark, J.J.; Zhang, X. Effect of using titanium interlayers on the properties of vitrified diamond tools. *Int. J. Comput. Mater. Sci. Surf. Eng.* **2010**, *3*, 86–94. [[CrossRef](#)]
19. Liu, X.; Wang, F.; Wang, W.; Wu, H. Interfacial strengthening and self-healing effect in graphene-copper nanolayered composites under shear deformation. *Carbon* **2016**, *107*, 680–688. [[CrossRef](#)]
20. Liu, X.; Wang, F.; Wu, H.; Wang, W. Strengthening metal nanolaminates under shock compression through dual effect of strong and weak graphene interface. *Appl. Phys. Lett.* **2014**, *104*, 231901. [[CrossRef](#)]
21. Steve, P. Fast parallel algorithms for short-range molecular dynamics. *J. Comput. Phys.* **1995**, *117*, 1–19.
22. Jain, A.; Ong, S.P.; Hautier, G.; Chen, W.; Richards, W.D.; Dacek, S.; Cholia, S.; Gunter, D.; Skinner, D.; Ceder, G.; et al. The Materials Project: A materials genome approach to accelerating materials innovation. *APL Mater.* **2013**, *1*, 011002. [[CrossRef](#)]
23. Zhao, H.; Aluru, N.R. Temperature and strain-rate dependent fracture strength of graphene. *J. Appl. Phys.* **2010**, *108*, 064321. [[CrossRef](#)]
24. Yi, L.; Yin, Z.; Zhang, Y.; Chang, T. A theoretical evaluation of the temperature and strain-rate dependent fracture strength of tilt grain boundaries in graphene. *Carbon* **2013**, *51*, 373–380. [[CrossRef](#)]
25. Fonseca, A.F.; Liang, T.; Zhang, D.; Choudhary, K.; Phillpot, S.R.; Sinnott, S.B. Graphene-Titanium Interfaces from Molecular Dynamics Simulations. *ACS Appl. Mater. Interfaces* **2017**, *9*, 33288–33297. [[CrossRef](#)]
26. Zhang, D.; Fonseca, A.F.; Liang, T.; Phillpot, S.R.; Sinnott, S.B. Dynamics of graphene/Al interfaces using COMB3 potentials. *Phys. Rev. Mater* **2019**, *3*, 114002. [[CrossRef](#)]
27. Jiang, T.; Zhang, X.; Vishwanath, S.; Mu, X.; Kanzyuba, V.; Sokolov, D.A.; Ptasinska, S.; Go, D.B.; Xing, H.G.; Luo, T. Covalent bonding modulated graphene-metal interfacial thermal transport. *Nanoscale* **2016**, *8*, 10993–11001. [[CrossRef](#)]
28. Cingolani, J.S.; Deimel, M.; Köcher, S.; Scheurer, C.; Reuter, K.; Andersen, M. Interface between graphene and liquid Cu from molecular dynamics simulations. *J. Chem. Phys.* **2020**, *153*, 074702. [[CrossRef](#)]
29. Lin, F.; Xiang, Y.; Shen, H.S. Tunable Positive/Negative Young's Modulus in Graphene—Based Metamaterials. *Adv. Theory Simul.* **2021**, *4*, 2000130. [[CrossRef](#)]
30. Sha, Z.; Branicio, P.; Pei, Q.; Sorkin, V.; Zhang, Y. A modified Tersoff potential for pure and hydrogenated diamond-like carbon. *Comput. Mater. Sci.* **2013**, *67*, 146–150. [[CrossRef](#)]
31. Mylvaganam, K.; Zhang, L. Ballistic resistance capacity of carbon nanotubes. *Nanotechnology* **2007**, *18*, 475701.
32. Hoover, W.G. Canonical dynamics: Equilibrium phase-space distributions. *Phys. Rev. A* **1985**, *31*, 1695. [[CrossRef](#)] [[PubMed](#)]
33. Verlet, L. Computer “experiments” on classical fluids. I. Thermodynamical properties of Lennard-Jones molecules. *Phys. Rev.* **1967**, *159*, 98. [[CrossRef](#)]
34. Diao, J.; Gall, K.; Dunn, M.L. Atomistic simulation of the structure and elastic properties of gold nanowires. *J. Mech. Phys. Solids* **2004**, *52*, 1935–1962. [[CrossRef](#)]
35. Xia, K.; Zhan, H.; Ji, A.; Shao, J.; Gu, Y.; Li, Z. Graphynes: An alternative lightweight solution for shock protection. *Beilstein J. Nanotechnol.* **2019**, *10*, 1588–1595. [[CrossRef](#)] [[PubMed](#)]
36. Xia, K.; Zhan, H.; Hu, D.; Gu, Y. Failure mechanism of monolayer graphene under hypervelocity impact of spherical projectile. *Sci. Rep.* **2016**, *6*, 33139. [[CrossRef](#)]
37. Yin, H.; Qi, H.J.; Fan, F.; Zhu, T.; Wang, B.; Wei, Y. Griffith Criterion for Brittle Fracture in Graphene. *Nano Lett.* **2015**, *15*, 1918–1924. [[CrossRef](#)]
38. Xia, K.; Zhan, H.; Zhang, X.; Li, Z. Graphdiyne family-tunable solution to shock resistance. *Mater. Res. Express.* **2020**, *7*, 115602. [[CrossRef](#)]
39. Liao, C.-Y.; Ma, C.-C. Transient behavior of a cantilever plate subjected to impact loading: Theoretical analysis and experimental measurement. *Int. J. Mech. Sci.* **2020**, *166*, 105217.
40. Wei, Y.; Zhan, H.; Xia, K.; Zhang, W.; Sang, S.; Gu, Y. Resonance of graphene nanoribbons doped with nitrogen and boron: A molecular dynamics study. *Beilstein J. Nanotechnol.* **2014**, *5*, 717–725.
41. Zheng, Z.; Zhan, H.; Nie, Y.; Xu, X.; Qi, D.; Gu, Y. Single layer diamond—A new ultrathin 2D carbon nanostructure for mechanical resonator. *Carbon* **2020**, *161*, 809–815. [[CrossRef](#)]
42. Hernandez, S.A.; Fonseca, A.F. Anisotropic elastic modulus, high Poisson's ratio and negative thermal expansion of graphynes and graphdienes. *Diam. Relat. Mater.* **2017**, *77*, 57–64. [[CrossRef](#)]
43. Zhang, Y.; Pei, Q.; Wang, C. Mechanical properties of graphynes under tension: A molecular dynamics study. *Appl. Phys. Lett.* **2012**, *101*, 081909. [[CrossRef](#)]
44. Lee, J.-H.; Loya, P.E.; Lou, J.; Thomas, E.L. Dynamic mechanical behavior of multilayer graphene via supersonic projectile penetration. *Science* **2014**, *346*, 1092–1096. [[CrossRef](#)] [[PubMed](#)]